OUKA
The University of Osaka
Institutional Knowledge Archive

Title	Effect of the OH functionalization on the catalytic activity of a single-atom catalyst
Author(s)	Zainul Abidin, Azim Fitri; Adhitya Gandaryus Saputro; Lorna Jeffery Minggu et al.
Citation	Philosophical transactions. Series A, Mathematical, physical, and engineering sciences. 2026, 384(2318), p. 20240475
Version Type	VoR
URL	https://hdl.handle.net/11094/104683
rights	This article is licensed under a Creative Commons Attribution 4.0 International License.
Note	

The University of Osaka Institutional Knowledge Archive : OUKA

https://ir.library.osaka-u.ac.jp/

The University of Osaka

PHILOSOPHICAL TRANSACTIONS A

royalsocietypublishing.org/journal/rsta

CC BY

Research

Cite this article: Abidin AFZ, Saputro AG, Minggu LJ, Yunus RM, Hamada I. 2026 Effect of the OH functionalization on the catalytic activity of a single-atom catalyst. *Phil. Trans. R. Soc. A* **384**: 20240475.
https://doi.org/10.1098/rsta.2024.0475

Received: 26 June 2025
Accepted: 16 September 2025

One contribution of 14 to a theme issue 'Surfaces, interfaces and heterogeneous catalysis'.

Subject Areas:
chemical physics, computational chemistry, physical chemistry, chemical physics, materials science

Keywords:
single atom catalyst, density functional theory, oxygen reduction reaction, implicit solvation

Authors for correspondence:
Azim Fitri Zainul Abidin
e-mail: azimfitre@ukm.edu.my
Ikutaro Hamada
e-mail: ihamada@prec.eng.osaka-u.ac.jp

Electronic supplementary material is available online at https://doi.org/10.6084/m9.figshare.c.8396019.

THE ROYAL SOCIETY PUBLISHING

Effect of the OH functionalization on the catalytic activity of a single-atom catalyst

Azim Fitri Zainul Abidin[1], Adhitya Gandaryus Saputro[2], Lorna Jeffery Minggu[1], Rozan Mohamad Yunus[1] and Ikutaro Hamada[3]

[1]Fuel Cell Institute, Universiti Kebangsaan Malaysia, Bangi, Selangor, Malaysia
[2]Institut Teknologi Bandung, Bandung, West Java, Indonesia
[3]Department of Precision Engineering, The University of Osaka, Suita, Osaka, Japan

IH, 0000-0001-5112-2452

The existence of the hydroxyl ligand on a single-atom catalyst embedded in graphene, especially Fe(OH)–N_4–C, is suggested to improve the oxygen reduction reaction (ORR) from the pristine Fe–N_4–C. However, the theoretical electrocatalytic activity of the ORR process is shown to be highly dependent on the electrolyte solution and the applied electrode potential. Herein, we performed the constant-potential simulation and microkinetic modelling to investigate the mechanism of ORR on well-studied Fe(OH)–N_4–C and Co(OH)–N_4–C catalysts and compared them with the pristine ones, using density functional theory calculation combined with the effective screening medium method and the reference interaction site model. It was found that the Fe(OH)–N_4–C and Co(OH)–N_4–C have comparable ORR activities to Fe–N_4–C and Co–N_4–C, and the calculated limiting potentials and half-wave potentials agree with the experimental values, in contrast to the results obtained using the constant-charge method (i.e. under the neutral condition) regardless of consideration of the solvation effect.

This article is part of the theme issue 'Surfaces, interfaces and heterogeneous catalysis'.

© 2026 The Authors. Published by the Royal Society under the terms of the Creative Commons Attribution License http://creativecommons.org/licenses/by/4.0/, which permits unrestricted use, provided the original author and source are credited.

Downloaded from http://royalsocietypublishing.org/rsta/article-pdf/doi/10.1098/rsta.2024.0475/6132976/rsta.2024.0475.pdf
by guest
on 08 May 2026

1. Introduction

The electrocatalytic oxygen reduction reaction (ORR) is a critical process in proton exchange membrane fuel cells and metal–air batteries for energy conversion [1–3]. However, the sluggish kinetic nature of the ORR at the cathode hampers its energy conversion efficiency [4]. Despite the high ORR activity demonstrated by the precious Pt-based catalysts, their widespread application is impeded by their exorbitant cost and scarcity [5]. Transition metal (TM) single-atom catalysts, mainly Fe and Co, embedded in N-doped graphitic materials (TM−N−C (TM = Fe, Co)), have emerged as viable substitutes for Pt to facilitate low temperature ORR [6–14]. Electrocatalytic activities of the Fe−N−C and Co−N−C are estimated by measuring the half-wave potentials ($E_{1/2}$) of ORR, which are as high as 0.75–0.83 V and 0.82–0.92 V for the former and the latter, respectively [10,15–18]. However, the catalytic activity and stability of these single atom catalysts still fall short compared with the Pt-based system [19–22]. To bridge this gap, various strategies have been devised, including the control of the local Fe- and Co-coordination environment [7,23–26], maximizing the active site density [9,27,28] and heteroatom doping with *p*-block element for surface functionalization [13,29–31]. Despite these efforts, achieving further optimization requires an atomic-level understanding of the electrochemical interface, including geometries, surface charges and electrolyte at the ORR reducing potentials [32,33]. According to the ex situ Fe K edge x-ray absorption spectroscopy and Mössbauer spectroscopy, it is suggested that a fourfold coordinated Fe/Co atom with pyridinic-N atoms in graphene, dubbed Fe−N_4−C and Co−N_4−C, serves as the main active site for this type of catalyst [34–38].

Recent studies employing density functional theory (DFT) calculations and computational hydrogen electrode (CHE) [39] model proposed the existence of an OH functionalization at the Fe/Co atom at the ORR reducing potential and TM(OH)−N_4−C moieties (TM = Fe,Co) as the active site for single-atom catalysts with high ORR activity [7,40]: Wang *et al.* [7] predicted the limiting potential (U_L) for the Fe−N_4–C model of 0.40 V, which is much smaller than experimental $E_{1/2}$. However, by employing the Fe(OH)−N_4–C model, they obtained theoretical U_L of 0.76 V. Furthermore, they performed the microkinetic modelling and predicted theoretical $E_{1/2}$ of 0.51 V and 0.88 V for Fe−N_4−C and Fe(OH)−N_4−C, respectively, supporting the presence of the OH functionalization at the ORR reducing potential. Yang *et al.* [41] performed DFT calculations focusing on Fe−N_4−C, where they predicted large U_L of approximately 0.84 V for Fe(OH)−N_4−C as compared with that for a plane active site of approximately 0.53 V. These results have also been supported by the work of Patniboon & Hansen [42], where they predicted U_L for Fe(OH)−N_4−C is as large as 0.67 V and 0.4 V for Fe−N_4−C. We also performed the calculations of the same systems and obtained consistent results [43]. Zhang *et al.* [44] also reported improved U_L of 0.91 V for Fe(OH)−N_4−C as compared with that of 0.60 V for Fe−N_4−C. In the case of Co, Patniboon & Hansen [42] reported U_L of 0.79 V for Co(OH)−N_4−C, which is slightly larger than that of 0.77 V for Co−N_4−C. However, Zhang *et al.* [44] reported a decrease in U_L in the case of Co: U_L for Co(OH)−N_4−C was calculated to be 0.82 V, while that for Co−N_4−C is 0.98 V. We also reported the results for Co−N_4−C and Co(OH)−N_4−C and found that the results depend on the exchange-correlation functional used. These studies indicate that the *OH functionalization may enhance the ORR activity of the single atom catalyst, especially for Fe−N_4−C, but for Co−N_4−C, the effect and the role of the OH functionalization need to be clarified. More recently, we studied ORR on TM−N_4−C (TM = Fe, Co) using DFT with an implicit solvation (IS) model at constant electrode potential [32]. We performed systematic calculations and clarified the roles of the solvent, electrolyte ions (within the IS model) and electrode potential. Furthermore, we obtained U_L's for Fe−N_4−C and Co−N_4−C, which are consistent with the experiment, even without the presence of the OH functionalization at the metal site. We attribute the origin of the discrepancies between the experiments and previous computational studies to surface charge at the ORR reducing potential. The results also motivated us to revisit TM(OH)−N_4−C and the role of the OH functionalization in ORR using the same computational framework as in our previous study [32].

Downloaded from http://royalsocietypublishing.org/rsta/article-pdf/doi/10.1098/rsta.2024.0475/6132976/rsta.2024.0475.pdf
by guest
on 08 May 2026

Herein, we use DFT and the effective screening medium method combined with the reference site interaction model (ESM-RISM), hybrid DFT and an IS model, which allows the calculations of electrode–electrolyte interfaces at a constant electrode potential, and investigate the mechanism of ORR on TM(OH)−N_4−C and the role of the OH functionalization.

2. Methods

(a) Computational details

All the DFT calculations in this work were performed using the projected augmented wave (PAW) [45] method as implemented in Quantum-ESPRESSO code [46,47]. The PAW potentials were adopted from pslibrary [48], which were generated using Perdew–Burke–Ernzerhof (PBE) generalized gradient approximation to the exchange-correlation (XC) functional [49]. Wave functions and augmentation charge density were expanded in terms of a plane wave basis set with the kinetic energy cut-offs of 80 and 800 Ry, respectively. To treat the Fermi level, the Marzari–Vanderbilt cold smearing with a smearing width of 0.02 Ry is used [50], as it has been validated to give reasonable results [43]. A 4×4 grid was used to generate **k**-points for the Brillouin zone sampling, as it was found to give reasonably accurate results [43]. A 8×8 **k**-points grid was used for the electronic structure analyses. The revised PBE (RPBE) XC functional of Hammer *et al.* [51] with Grimme's dispersion correction was chosen for its balance of accuracy and computational efficiency. We confirmed that RPBE-D3 shows similar accuracy to the BEEF-vdW functional [43]. The TM(OH)−N_4−C was modelled using a (5×5) graphene surface unit cell, where we removed two carbon atoms to anchor a single Fe or Co atom, replaced the four surrounding four-coordinate carbon atoms with nitrogen atoms to form a nitrogen-doped coordination environment, and added an OH below the Fe/Co atom in the axial position to simulate the active site for this catalytic study. The TM(OH)−N_4−C was constructed in accordance with the recent theoretical study by Wang *et al.* [7] and the experimental observations reported by Jia *et al.* [38] ensuring consistency with their findings on the active site structure of similar systems. TM(OH)−N_4−C structure and all of the reaction intermediates were then modelled using the vacuum/slab/solvent boundary condition in ESM. The graphene surface was in contact with 0.5 M HCl solution at 298.15 K, which was described using RISM. All the reaction intermediates (*OOH, *O and *OH) on TM(OH)−N_4−C were fully optimized until the residual forces on the constituent atom became less than 2.57×10^{-2} eV/Å. The kinetic energy cut-off for the solvent correlation functions was set to 160 Ry. The electrolyte solution and its interface with TM(OH)−N_4−C were described using the Lennard–Jones potential with modified parameters as detailed in Ref. [32]. In this work, only 0.5 M HCl solution was used to represent an acidic environment, as the electrolyte concentration is shown to have insignificant impact on the reaction mechanism within the ESM-RISM framework [32]. While the accuracy of ESM-RISM for TM(OH)-N_4-C has yet to be assessed, comparative evaluations of solvation models, including ESM-RISM, can be found in Ref. [52]. We performed calculations of TM(OH)−N_4−C/HCl solution interface under the charge-neutral/potential of zero charge (constant-N_e) and constant-electrode potential (constant-μ_e) conditions for comparison. For the former, the effect of the electrode potential on the free energy was considered in the framework of CHE. See Ref. [32] for further details of the calculation. We also construct the microkinetic model to further analyse the ORR polarization curve and surface coverage pattern within the TM−N_4−C and TM(OH)−N_4−C surfaces, using the calculated Gibbs free energies as inputs [7,25,37,53–56]. The computational details of the ESM–RISM method and microkinetic analysis are provided in the electronic supplementary material.

Downloaded from http://royalsocietypublishing.org/rsta/article-pdf/doi/10.1098/rsta.2024.0475/6132976/rsta.2024.0475.pdf
by guest
on 08 May 2026

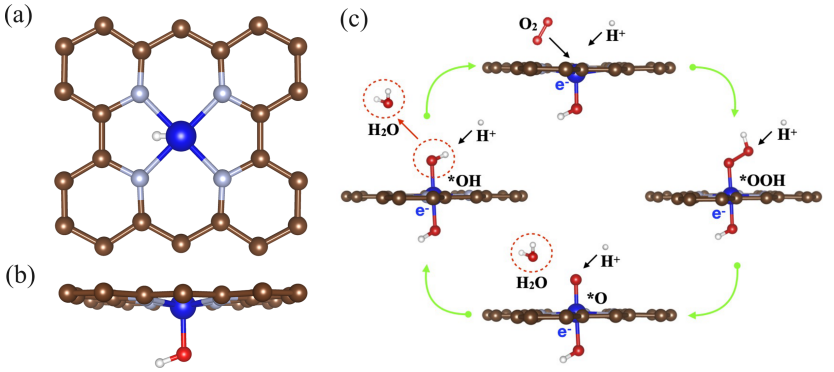


Figure 1. (*a*) Top and (*b*) side views of the structure of the TM(OH)-N_4-C (TM = Fe, Co) active site. (*c*) Schematic of the ORR reaction process on the active site through the associative pathway. White, brown, grey, red and blue spheres represent H, C, N, O and TM (TM = Fe, Co), respectively. The structures were visualized using VESTA [57].

Table 1. The potential-determining step (PDS), limiting potential (U_L) and overpotential (η) of ORR estimated for TM(OH)–N_4–C in vacuum [43] and those for TM(OH)–N_4–C in contact with 0.5 M HCl solution obtained using the constant-N_e and constant-μ_e methods with ESM-RISM.

	constant-N_e (vacuum)	constant-N_e (ESM-RISM)	constant-μ_e (ESM-RISM)
Fe(OH)–N_4–C			
PDS	$^*OH \rightarrow H_2O$ (ΔG_4)	$^*OH \rightarrow H_2O$ (ΔG_4)	$^*OH \rightarrow H_2O$ (ΔG_4)
U_L	0.84 V	0.60 V	0.80 V
η	0.39 V	0.63 V	0.43 V
Co(OH)–N_4–C			
PDS	$O_2 \rightarrow OOH$ (ΔG_1)	$^*OH \rightarrow H_2O$ (ΔG_4)	$^*OH \rightarrow H_2O$ (ΔG_4)
U_L	0.89	0.74 V	0.83 V
η	0.34	0.49 V	0.44 V

3. Results and discussion

We first optimized the Fe(OH)–N_4–C and Co(OH)–N_4–C structures without and with the ORR intermediates in a vacuum (figure 1). The structures are then used to further calculate the ORR activity through the constant-N_e and constant-μ_e approaches using ESM-RISM. Figure 2 shows the free energy diagrams of ORR for the Fe(OH)–N_4–C and Co(OH)–N_4–C obtained using these two approaches. The potential determining step (PDS), U_L and overpotential (η) are summarized in table 1, along with those for the vacuum and constant-N_e condition. The effect of electrolyte with the constant-N_e approach is found important as the PDS changes from $O_2 \rightarrow ^*OOH$ (ΔG_1) to $^*OH \rightarrow H_2O$ (ΔG_4) in the case of the Co(OH)–N_4–C. However, the PDS remains to be $^*OH \rightarrow H_2O$ (ΔG_4) in the case of the Fe(OH)–N_4–C. Furthermore, the associated U_L (η) changes from 0.84 to 0.60 V (0.39–0.63 V) and 0.89 to 0.74 V (0.34–0.49 V) for the Fe(OH)–N_4–C and Co(OH)–N_4–C, respectively, upon inclusion of the 0.5 M HCl solution. The effect of electrolytes is found crucial in estimating the ORR activity, as it can change the PDS and U_L and η for both Fe(OH)–N_4–C and Co(OH)–N_4–C from those obtained using the vacuum condition. However, we note that the electrolyte concentration as well as the type of the solution were not significant within the ESM-RISM frameworks [43].

With the constant-N_e method, the predicted U_L (η) for Co(OH)–N_4–C of 0.74 V (0.49 V) is significantly higher (lower) than that of for Fe(OH)–N_4–C of 0.60 V (0.63 V), indicating that the

Downloaded from http://royalsocietypublishing.org/rsta/article-pdf/doi/10.1098/rsta.2024.0475/6132976/rsta.2024.0475.pdf
by guest
on 08 May 2026

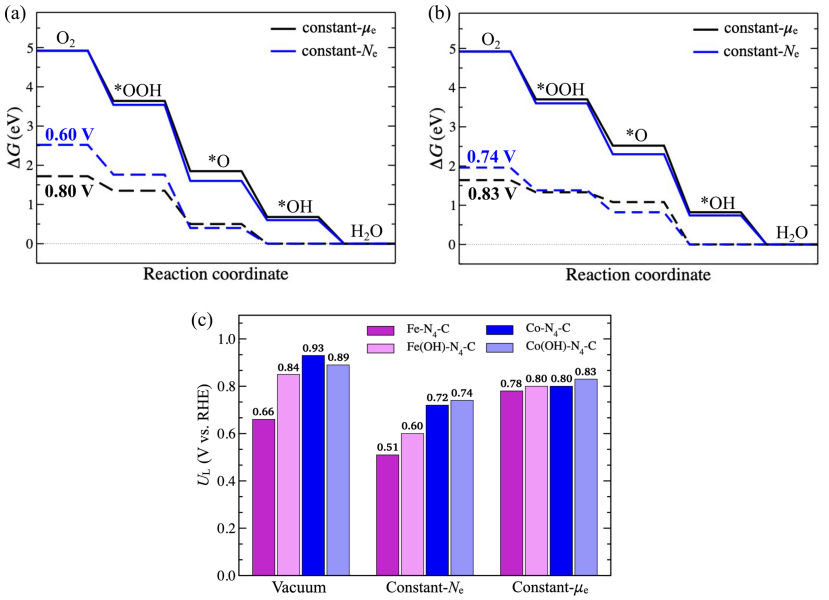


Figure 2. Calculated free energy diagram of ORR through the associative pathway for (*a*) Fe(OH)−N_4−C and (*b*) Co(OH)−N_4−C. The result obtained using constant-μ_e and constant-N_e are plotted with black and blue solid lines, while the dashed line represents the limiting potential (U_L) for both constant-μ_e and constant-N_e methods. (*c*) Calculated U_L for both TM(OH)−N_4−C and TM−N_4−C with three different methods considered in this work. The results for TM−N_4−C in the vacuum condition are taken from Ref. [43], and those with the constant-μ_e and constant-N_e methods are taken from Ref. [32].

former is more reactive than the latter. These results are consistent with those we calculated [32] for TM−N_4−C, where U_L (η) is 0.72 V (0.51 V) and 0.51 V (0.72 V) for Co−N_4−C and Fe−N_4−C, respectively, with the PDS on both surfaces being *OH → H_2O. However, with the OH functionalization, the η values for the Fe(OH)−N_4−C and Co(OH)−N_4−C are slightly lowered, indicating that the activity for the latter catalyst is improved from the former.

Furthermore, we performed calculations using the constant-μ_e method, where the effect of the electrolyte and the electrode potential is automatically included in the self-consistent field calculation. With this approach, we found that PDS for both Fe(OH)−N_4−C and Co(OH)−N_4−C remains to be *OH→H_2O (ΔG_4). However, U_L (η) is predicted to be 0.80 V (0.43 V) and 0.83 V (0.44 V) for the Fe(OH)−N_4−C and Co(OH)−N_4−C, respectively. These results indicate that the ORR performance of Fe(OH)−N_4−C and Co(OH)−N_4−C are comparable, in contrast to the constant-N_e results, in which the activity of Co(OH)−N_4−C is predicted to be higher than that of Fe(OH)−N_4−C. The U_L (η) values for Fe(OH)−N_4−C and Co(OH)−N_4−C are also found comparable to those of Fe−N_4−C of 0.78 V (0.45 V) and Co−N_4−C 0.80 V (0.43 V), which are lower by 0.02 and 0.03 V, respectively. We note, however, that the predicted PDSs are different, which are O → OH and O_2 →* OOH for Fe−N_4−C and Co−N_4−C, respectively. These results indicate that, using the constant-μ_e method with ESM-RISM, the OH functionalization does not contribute to significant improvement to the activity of Fe−N_4−C and Co−N_4−C as we have observed with the constant-N_e method. The U_L value predicted using the constant-μ_e method for the Fe(OH)−N_4−C (Co(OH)−N_4−C) is closer to the experimental $E_{1/2}$ values of 0.75–0.83 V (0.82–0.92 V) [10,15–18] than that using the constant-N_e method. We concluded that with the constant-μ_e method, the predicted activity of the TM−N_4−C and TM(OH)−N_4−C are comparable, with the U_L values for the former slightly lower than the latter.

In trying to understand the origin of the difference between the results obtained using these methods, we calculated the ΔG's for the ORR intermediates as functions of electrode potential

Downloaded from http://royalsocietypublishing.org/rsta/article-pdf/doi/10.1098/rsta.2024.0475/6132976/rsta.2024.0475.pdf
by guest
on 08 May 2026

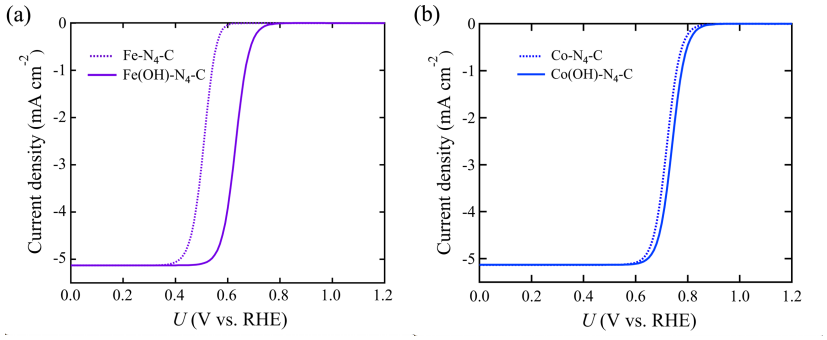


Figure 3. Simulated ORR polarization curves for (a) Fe—N_4—C and Fe(OH)—N_4—C and (b) Co—N_4—C and Co(OH)—N_4—C, based on the constant-N_e method.

with the constant-μ_e and the constant-N_e method from 0 to 1.23 V (electronic supplementary material). As in the cases for TM − N_4 − C, ΔG's depend linearly on the electrode potential. However, unlike the CHE approach, the linear coefficients for the electrode potential deviate from 1, leading to different ORR mechanisms using the constant-μ_e method than the constant-N_e method. The discrepancies between the results obtained using the constant-μ_e and constant-N_e methods primarily originate from the charge of the system: in contrast to the constant-N_e method, where the whole system is kept neutral, the charge of the system varies depending on the electrode potential and different from 0 (neutral) even at zero potential (0 V with respect to the reversible hydrogen electrode potential) (electronic supplementary material). This leads to different slopes of ΔG's, thereby different ORR mechanisms and limiting potentials (overpotentials).

We also analyse the electronic structures of TM−N_4 − C and TM(OH)−N_4 − C to gain insight into the significance of the OH functionalization in their ORR activities (electronic supplementary material). We focused on OH-adsorbed TM−N_4 − C and TM(OH)−N_4 − C and found that their densities of states near the Fermi level (E_F) look similar, regardless of the presence of the OH ligand. In particular, the p_y orbitals of adsorbed OH exhibit similar density of states near E_F, which may explain the stability of OH on both active sites (i.e. those with and without the OH functionalization) and resulting U_L and η.

Theoretical ORR polarization curves for TM−N_4−C and TM(OH)−N_4−C were calculated using both the constant-N_e and constant-μ_e methods, as shown in figures 3 and 4, respectively. Using the constant-N_e method, Fe(OH)−N_4−C is predicted to exhibit theoretical $E_{1/2}$ of approximately 0.65 V, which is slightly higher than that of Fe−N_4−C (approx. 0.54 V). By contrast, the $E_{1/2}$ values for Co(OH)−N_4−C (approx. 0.78 V) and Co−N_4−C (approx. 0.76 V) are nearly identical. These $E_{1/2}$ values differ from those reported in the literature [7], presumably due to the different implicit solvation methods used and the resulting ORR mechanism from those based on the present work. Using the constant-μ_e method, Fe(OH)−N_4−C is predicted to exhibit $E_{1/2}$ of approximately 0.88 V, which is comparable to Fe−N_4−C (approx. 0.86 V). Similarly, Co(OH)−N_4−C exhibits $E_{1/2}$ of approximately 0.91 V, closely matches with that of Co−N_4−C (approx. 0.88 V). These predictions support our free energy-based results that both Fe(OH)−N_4−C and Co(OH)−N_4−C display ORR activities similar to their pristine counterparts, with the effect of the OH-functionalization on the Co−N_4−C being less significant than on Fe−N_4−C.

The surface coverages of the ORR intermediates were also calculated as functions of electrode potential using the constant-N_e and constant-μ_e methods, as shown in figures 5 and 6, respectively. At a low potential, the surface coverage is primarily dominated by those of the free sites (*) across all TM−N_4−C's and TM(OH)−N_4−C's. For Fe−N_4−C and Fe(OH)−N_4−C using the constant-N_e method, surface poisoning is predicted to begin at approximately 0.58 and 0.97 V, respectively, where *OH becomes the dominant species. At higher potential (above approx. 0.70 V for Fe−N_4−C and approx. 0.90 for Fe(OH)−N_4−C), *O replaces *OH as the dominant species.

Downloaded from http://royalsocietypublishing.org/rsta/article-pdf/doi/10.1098/rsta.2024.0475/6132976/rsta.2024.0475.pdf
by guest
on 08 May 2026

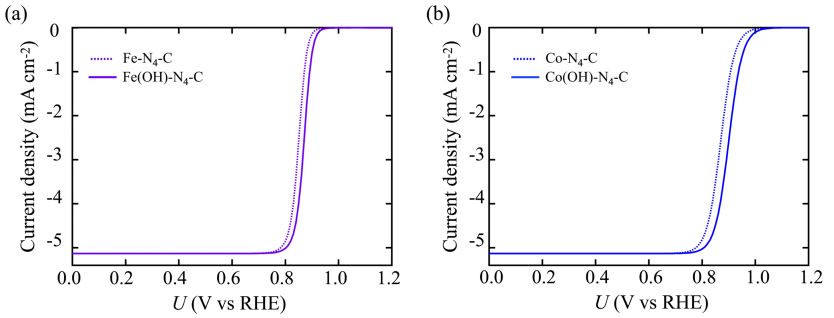


Figure 4. Simulated ORR polarization curves for (a) Fe—N_4—C and Fe(OH)—N_4—C and (b) Co—N_4—C and Co(OH)—N_4—C, based on the constant-μ_e method.

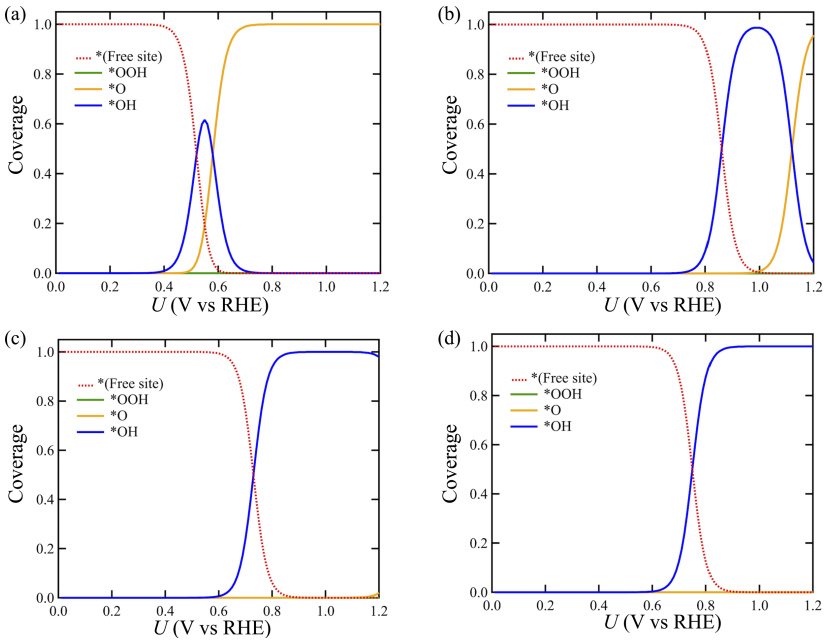


Figure 5. Surface coverages as functions of electrode potential *U* obtained using the constant-N_e method for (*a*) Fe—N_4—C, (*b*) Fe(OH)—N_4—C, (*c*) Co—N_4—C and (*d*) Co(OH)—N_4—C.

Similarly, for Co–N_4–C and Co(OH)-N_4-C, the *OH begins to appear at around 0.6 V and becomes the dominant species above 0.8 and 0.83 V, respectively. However, under the constant-μ_e method, all of TM–N_4–C and TM(OH)–N_4–C surfaces become dominated by *OH at potentials above 0.80 V. It is also observed that for Co–N_4–C, both without and with OH-terminated, the intermediate coverage pattern remains nearly identical using both methods. This results in a similar $E_{1/2}$ prediction compared with Fe–N_4–C and Fe(OH)–N_4–C.

4. Conclusion

We performed DFT calculations and microkinetic modelling to study the electrochemical ORR mechanism for TM–N_4 – C (TM = Fe, Co) functionalized by the OH group [TM(OH)–N_4–C] in an acidic solution using ESM-RISM. In particular, we focus on the role of the OH functionalization in ORR on TM(OH)–N_4 – C, which has been suggested to be the origin of the high ORR activity of TM–N_4 – C. We found that with the constant-potential method, i.e. under the applied

Downloaded from http://royalsocietypublishing.org/rsta/article-pdf/doi/10.1098/rsta.2024.0475/6132976/rsta.2024.0475.pdf
by guest
on 08 May 2026

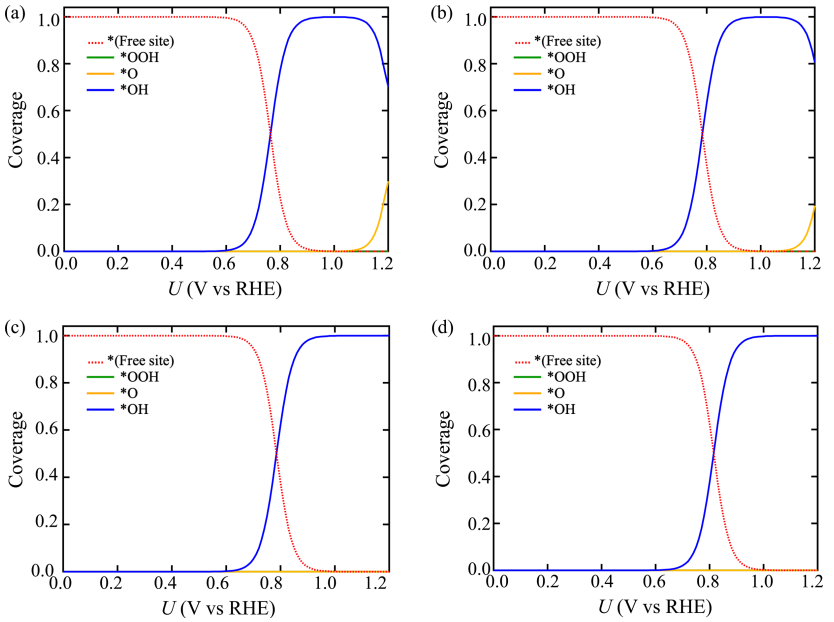


Figure 6. Surface coverage as a function of electrode potential U with the constant-μ_e method for associative mechanism on (*a*) Fe—N_4—C, (*b*) Fe(OH)—N_4—C, (*c*) Co—N_4—C and (*d*) Co(OH)—N_4—C.

electrode potential and variable surface charge, the OH functionalization does not lead to significant enhancement of the ORR activity of TM(OH)-N_4-C, which is in sharp contrast to the results obtained with the conventional CHE model under the neutral condition. Our study highlights the importance of using the constant-potential calculation in the investigation of electrochemical reactions and underscores the need for further studies of electrochemical ORR on a wide range of catalytic materials beyond single-atom catalysts. Investigation of the roles of other functionalization groups in electrochemical ORR, such as acid anions on the single-atom catalysts using the constant-potential method, is of great interest and will be the focus of our future study.

Data accessibility. The data underlying this study are openly available in Materials Cloud [58].

Supplementary material is available online [59].

Declaration of AI use. We have not used AI-assisted technologies in creating this article.

Authors' contributions. A.F.Z.A.: conceptualization, formal analysis, investigation, validation, visualization, writing—original draft, writing—review and editing; A.G.S.: investigation, validation; L.J.M.: investigation, validation; R.M.Y.: investigation, validation; I.H.: conceptualization, formal analysis, investigation, methodology, supervision, validation, writing—review and editing.

All authors gave final approval for publication and agreed to be held accountable for the work performed therein.

Conflict of interest declaration. We declare we have no competing interests.

Funding. This work was supported by the Universiti Kebangsaan Malaysia Research Grant through Geran Galakkan Penyelidik Muda (Grant No. GGPM-2024-041).

Acknowledgements. A part of the calculations was performed using the facilities of the Supercomputer Center, the Institute for Solid State Physics, The University of Tokyo, and the D3 Center, The University of Osaka.

References

1. Debe MK. 2012 Electrocatalyst approaches and challenges for automotive fuel cells. *Nature* **486**, 43–51. (doi:10.1038/nature11115)
2. Steele BC, Heinzel A. 2001 Materials for fuel-cell technologies. *Nature* **414**, 345–352. (doi:10.1038/35104620)

Downloaded from http://royalsocietypublishing.org/rsta/article-pdf/doi/10.1098/rsta.2024.0475/6132976/rsta.2024.0475.pdf
by guest
on 08 May 2026

3. Letchumanan I, Karim NA, Yunus RM, Mastar MS *et al*. 2024 Advancements in electrocatalyst architecture for enhanced oxygen reduction reaction in anion exchange membrane fuel cells: a comprehensive review. *Int. J. Hydrog. Energy* **104**, 527–546. (doi:10.1016/j.ijhydene.2024.05.455)
4. Jasinski R. 1964 A new fuel cell cathode catalyst. *Nature* **201**, 1212–1213. (doi:10.1038/2011212a0)
5. Lin R, Cai X, Zeng H, Yu Z. 2018 Stability of high-performance pt-based catalysts for oxygen reduction reactions. *Adv. Mater*. **30**, e1705332. (doi:10.1002/adma.201705332)
6. Chen Y *et al*. 2017 Isolated single iron atoms anchored on N-doped porous carbon as an efficient electrocatalyst for the oxygen reduction reaction. *Angew. Chem. Int. Ed*. **56**, 6937–6941. (doi:10.1002/anie.201702473)
7. Wang Y, Tang YJ, Zhou K. 2019 Self-adjusting activity induced by intrinsic reaction intermediate in Fe–N–C single-atom catalysts. *J. Am. Chem. Soc*. **141**, 14115–14119. (doi:10.1021/jacs.9b07712)
8. Zhou Y, Yu Y, Ma D, Foucher AC, Xiong L, Zhang J, Stach EA, Yue Q, Kang Y. 2021 Atomic Fe dispersed hierarchical mesoporous Fe–N–C nanostructures for an efficient oxygen reduction reaction. *ACS Catal*. **11**, 74–81. (doi:10.1021/acscatal.0c03496)
9. Zhang H *et al*. 2017 Single atomic iron catalysts for oxygen reduction in acidic media: particle size control and thermal activation. *J. Am. Chem. Soc*. **139**, 14143–14149. (doi:10.1021/jacs.7b06514)
10. Wang J *et al*. 2017 Design of N-coordinated dual-metal sites: a stable and active Pt-free catalyst for acidic oxygen reduction reaction. *J. Am. Chem. Soc*. **139**, 17281–17284. (doi:10.1021/jacs.7b10385)
11. Strickland K, Miner E, Jia Q, Tylus U, Ramaswamy N, Liang W, Sougrati MT, Jaouen F, Mukerjee S. 2015 Highly active oxygen reduction non-platinum group metal electrocatalyst without direct metal–nitrogen coordination. *Nat. Commun*. **6**, 7343. (doi:10.1038/ncomms8343)
12. Fitri A, Loh KS, Puspasari I, Mohamad AB. 2017 Cobalt-doped carbon xerogel with different initial pH values toward oxygen reduction. *AIP Conf. Proc* **1901**, 020027. (doi:10.1063/1.5010464)
13. Aziz FFA, Timmiati SN, Samidin S, Fauzi AA, Wan Isahak WNR, Chitraningrum N, Jalil AA, Zainul Abidin AF, Salehmin MNI. 2025 Insight into supported single-atom catalysts design for thermocatalytic, electrocatalytic and photocatalytic conversion CO_2 to CH_4. *J. Ind. Eng. Chem*. **145**, 99–122. (doi:10.1016/j.jiec.2024.10.063)
14. Azhar N, Ng WS, Mohd Shah NRA, Zainul Abidin AF, Arifin K, Loh KS, Wong WY, Mohamad Yunus R. 2025 Recent progress and a new perspective of borophene-based catalyst for hydrogen energy applications: a review. *Mater. Today Chem*. **46**, 102716. (doi:10.1016/j.mtchem.2025.102716)
15. Xie X *et al*. 2020 Performance enhancement and degradation mechanism identification of a single-atom Co–N–C catalyst for proton exchange membrane fuel cells. *Nat. Catal*. **3**, 1044–1054. (doi:10.1038/s41929-020-00546-1)
16. Zhou Y, Chen G, Wang Q, Wang D, Tao X, Zhang T, Feng X, Müllen K. 2021 Fe-N-c electrocatalysts with densely accessible Fe-N_4 sites for efficient oxygen reduction reaction. *Adv. Funct. Mater*. **31**, 2102420. (doi:10.1002/adfm.202102420)
17. Jiao L *et al*. 2021 Chemical vapour deposition of Fe-N-C oxygen reduction catalysts with full utilization of dense Fe-N_4 sites. *Nat. Mater*. **20**, 1385–1391. (doi:10.1038/s41563-021-01030-2)
18. Yin S *et al*. 2020 Construction of highly active metal-containing nanoparticles and FeCo-N_4 composite sites for the acidic oxygen reduction reaction. *Angew. Chem. Int. Ed*. **132**, 22160–22163. (doi:10.1002/ange.202010013)
19. Hutchison P, Rice PS, Warburton RE, Raugei S, Hammes-Schiffer S. 2022 Multilevel computational studies reveal the importance of axial ligand for oxygen reduction reaction on Fe–N–C materials. *J. Am. Chem. Soc*. **144**, 16524–16534. (doi:10.1021/jacs.2c05779)
20. Raduwan NF, Shaari N, Kamarudin SK, Masdar MS, Yunus RM. 2023 Structural transformation doubly triggered by hydrothermal temperature and reaction time in 3D mixed transition metal oxide: great enhancement of pore size distribution and specific surface area. *Int. J. Hydrogen Energy* **48**, 27289–27297. (doi:10.1016/j.ijhydene.2023.03.394)
21. Sudarsono W, Wong WY, Loh KS, Kok KY, Syarif N, Abidin AFZ, Hamada I. 2022 Elucidating the roles of the Fe-Nx active sites and pore characteristics on Fe-Pani-biomass-derived

Downloaded from http://royalsocietypublishing.org/rsta/article-pdf/doi/10.1098/rsta.2024.0475/6132976/rsta.2024.0475.pdf
by guest
on 08 May 2026

RGO as oxygen reduction catalysts in PEMFCs. *Mater. Res. Bull.* **145**, 111526. (doi:10.1016/j.materresbull.2021.111526)
22. Anuar S, Loh K, Samad S, Abidin AZ, Wong W, Mohamad A, Lee T. 2020 Effect of carbon supports on oxygen reduction reaction of iron/cobalt electrocatalyst. *Int. J. Nanoelectron. Mater.* **13**, 225–232.
23. Gong L *et al*. 2020 Bridge bonded oxygen ligands between approximated FeN_4 sites confer catalysts with high ORR performance. *Angew. Chem. Int. Ed.* **132**, 14027–14032. (doi:10.1002/ange.202004534)
24. Ramaswamy N, Tylus U, Jia Q, Mukerjee S. 2013 Activity descriptor identification for oxygen reduction on nonprecious electrocatalysts: linking surface science to coordination chemistry. *J. Am. Chem. Soc.* **135**, 15443–15449. (doi:10.1021/ja405149m)
25. Rebarchik M, Bhandari S, Kropp T, Mavrikakis M. 2020 How noninnocent spectator species improve the oxygen reduction activity of single-atom catalysts: microkinetic models from first-principles calculations. *ACS Catal.* **10**, 9129–9135. (doi:10.1021/acscatal.0c01642)
26. Marshall-Roth T, Libretto NJ, Wrobel AT, Anderton KJ, Pegis ML, Ricke ND, Voorhis TV, Miller JT, Surendranath Y. 2020 A pyridinic Fe-N_4 macrocycle models the active sites in Fe/N-doped carbon electrocatalysts. *Nat. Commun.* **11**, 5283. (doi:10.1038/s41467-020-18969-6)
27. Jin Z, Li P, Meng Y, Fang Z, Xiao D, Yu G. 2021 Understanding the inter-site distance effect in single-atom catalysts for oxygen electroreduction. *Nat. Catal.* **4**, 615–622. (doi:10.1038/s41929-021-00650-w)
28. Xiao M *et al*. 2019 Climbing the apex of the ORR volcano plot via binuclear site construction: electronic and geometric engineering. *J. Am. Chem. Soc.* **141**, 17763–17770. (doi:10.1021/jacs.9b08362)
29. Mun Y, Lee S, Kim K, Kim S, Lee S, Han JW, Lee J. 2019 Versatile strategy for tuning ORR activity of a single Fe-N_4 site by controlling electron-withdrawing/donating properties of a carbon plane. *J. Am. Chem. Soc.* **141**, 6254–6262. (doi:10.1021/jacs.8b13543)
30. Zhu X, Yan J, Gu M, Liu T, Dai Y, Gu Y, Li Y. 2019 Activity origin and design principles for oxygen reduction on dual-metal-site catalysts: a combined density functional theory and machine learning study. *J. Phys. Chem. Lett.* **10**, 7760–7766. (doi:10.1021/acs.jpclett.9b03392)
31. Lefèvre M, Proietti E, Jaouen F, Dodelet JP. 2009 Iron-based catalysts with improved oxygen reduction activity in polymer electrolyte fuel cells. *Science* **324**, 71–74. (doi:10.1126/science.1170051)
32. Abidin AFZ, Hamada I. 2023 Oxygen reduction reaction on single-atom catalysts from density functional theory calculations combined with an implicit solvation model. *J. Phys. Chem. C.* **127**, 13623–13631. (doi:10.1021/acs.jpcc.3c02224)
33. Weitzner SE, Akhade SA, Varley JB, Wood BC, Otani M, Baker SE, Duoss EB. 2020 Toward engineering of solution microenvironments for the CO_2 reduction reaction: unraveling pH and voltage effects from a combined density-functional-continuum theory. *J. Phys. Chem. Lett.* **11**, 4113–4118. (doi:10.1021/acs.jpclett.0c00957)
34. Kramm UI, Herrmann-Geppert I, Behrends J, Lips K, Fiechter S, Bogdanoff P. 2016 On an easy way to prepare metal-nitrogen doped carbon with exclusive presence of MeN4-type sites active for the ORR. *J. Am. Chem. Soc.* **138**, 635–640. (doi:10.1021/jacs.5b11015)
35. Sa YJ. 2016 A general approach to preferential formation of active Fe–Nx sites in Fe–N/C electrocatalysts for efficient oxygen reduction reaction. *J. Am. Chem. Soc* **138**, 15046–15056. (doi:10.1021/jacs.6b09470)
36. Martini A, Hursán D, Timoshenko J, Rüscher M, Haase F, Rettenmaier C, Ortega E, Etxebarria A, Roldan Cuenya B. 2023 Tracking the evolution of single-atom catalysts for the CO_2 electrocatalytic reduction using operando X-ray absorption spectroscopy and machine learning. *J. Am. Chem. Soc.* **145**, 17351–17366. (doi:10.1021/jacs.3c04826)
37. Huang Z, Tang Q. 2022 Axial coordination effect on the oxygen reduction reaction of FeN_4 electrocatalysts based on grand canonical density functional theory. *J. Phys. Chem. C.* **126**, 21606–21615. (doi:10.1021/acs.jpcc.2c06682)
38. Jia Q *et al*. 2015 Experimental observation of redox-induced Fe-N switching behavior as a determinant role for oxygen reduction activity. *ACS Nano* **9**, 12496–12505. (doi:10.1021/acsnano.5b05984)

Downloaded from http://royalsocietypublishing.org/rsta/article-pdf/doi/10.1098/rsta.2024.0475/6132976/rsta.2024.0475.pdf
by guest
on 08 May 2026

39. Nørskov JK, Rossmeisl J, Logadottir A, Lindqvist L, Kitchin JR, Bligaard T, Jónsson H. 2004 Origin of the overpotential for oxygen reduction at a fuel-cell cathode. *J. Phys. Chem. B* **108**, 17886–17892. (doi:10.1021/jp047349j)
40. Mao K, Yang L, Wang X, Wu Q, Hu Z. 2020 Identifying iron–nitrogen/carbon active structures for oxygen reduction reaction under the effect of electrode potential. *J. Phys. Chem. Lett*. **11**, 2896–2901. (doi:10.1021/acs.jpclett.0c00428)
41. Yang X, Xia D, Kang Y, Du H, Kang F, Gan L, Li J. 2020 Unveiling the axial hydroxyl ligand on Fe-N_4-C electrocatalysts and its impact on the pH-dependent oxygen reduction activities and poisoning kinetics. *Adv. Sci.***7**, 2000176. (doi:10.1002/advs.202000176)
42. Patniboon T, Hansen HA. 2021 Acid-stable and active M–N–C catalysts for the oxygen reduction reaction: the role of local structure. *ACS Catal*. **11**, 13102–13118. (doi:10.1021/acscatal.1c02941)
43. Abidin AFZ, Hamada I. 2022 Comparative density functional theory study for predicting oxygen reduction activity of single-atom catalyst. *Surf. Sci*. **724**, 122144. (doi:10.1016/j.susc.2022.122144)
44. Zhang C, Dai Y, Sun Q, Ye C, Lu R, Zhou Y, Zhao Y. 2022 Strategy to weaken the oxygen adsorption on single-atom catalysts towards oxygen-involved reactions. *Mater. Today Adv* **16**, 100280. (doi:10.1016/j.mtadv.2022.100280)
45. Blöchl PE. 1994 Projector augmented-wave method. *Phys. Rev. B* **50**, 17953–17979. (doi:10.1103/PhysRevB.50.17953)
46. Giannozzi P *et al*. 2009 Quantum espresso: a modular and open-source software project for quantum simulations of materials. *J. Phys.: Condens. Matter* **21**, 395502. (doi:10.1088/0953-8984/21/39/395502)
47. Giannozzi P *et al*. 2017 Advanced capabilities for materials modelling with Quantum ESPRESSO. *J. Phys.: Condens. Matter* **29**, 465901. (doi:10.1088/1361-648X/aa8f79)
48. Dal Corso A. 2014 Pseudopotentials periodic table: from H to Pu. *Comput. Mater. Sci*. **95**, 337–350. (doi:10.1016/j.commatsci.2014.07.043)
49. Perdew JP, Burke K, Ernzerhof M. 1996 Generalized gradient approximation made simple. *Phys. Rev. Lett*. **77**, 3865–3868. (doi:10.1103/PhysRevLett.77.3865)
50. Marzari N, Vanderbilt D, De Vita A, Payne MC. 1999 Thermal contraction and disordering of the Al(110) surface. *Phys. Rev. Lett*. **82**, 3296–3299. (doi:10.1103/PhysRevLett.82.3296)
51. Hammer B, Hansen LB, Nørskov JK. 1999 Improved adsorption energetics within density-functional theory using revised Perdew-Burke-Ernzerhof functionals. *Phys. Rev. B* **59**, 7413–7421. (doi:10.1103/PhysRevB.59.7413)
52. Maldonado AM, Hagiwara S, Choi TH, Eckert F, Schwarz K, Sundararaman R, Otani M, Keith JA. 2021 Quantifying uncertainties in solvation procedures for modeling aqueous phase reaction mechanisms. *J. Phys. Chem. A* **125**, 154–164. (doi:10.1021/acs.jpca.0c08961)
53. Saputro AG, Fajrial AK, Maulana AL, Fathurrahman F, Agusta MK, Akbar FT, Dipojono HK. 2020 Dissociative oxygen reduction reaction mechanism on the neighboring active sites of a boron-doped pyrolyzed Fe–N–C catalyst. *J. Phys. Chem. C*. **124**, 11383–11391. (doi:10.1021/acs.jpcc.0c00632)
54. Rebarchik M, Bhandari S, Kropp T, Mavrikakis M. 2023 Insights into the oxygen evolution reaction on graphene-based single-atom catalysts from first-principles-informed microkinetic modeling. *ACS Catal*. **13**, 5225–5235. (doi:10.1021/acscatal.3c00474)
55. Li B, Shi C, Zhao N, Liu E. 2023 Hydrogen-bond-promoted ORR mechanism in P-doped Fe–N–C materials. *J. Phys. Chem. C*. **127**, 1023–1031. (doi:10.1021/acs.jpcc.2c07160)
56. Nuruddin A, Saputro AG, Maulana AL, Rusydi F, Akbar FT, Yudistira HT, Dipojono HK. 2024 Selectivity of CO_2 reduction reaction to CO on the graphitic edge active sites of Fe-single-atom and dual-atom catalysts: a combined DFT and microkinetic modeling. Carbon Resour. Convers. **7**, 100185. (doi:10.1016/j.crcon.2023.05.004)
57. Momma K, Izumi F. 2011 *VESTA 3* for three-dimensional visualization of crystal, volumetric and morphology data. *J. Appl. Crystallogr*. **44**, 1272–1276. (doi:10.1107/S0021889811038970)
58. Abidin AFZ, Gandaryus SA, Jeffery ML, Yunus RM, Ikutaro H. 2025 Data for: Effect of the OH functionalization on the catalytic activity of single-atom catalyst. Materials Cloud Archive. 2025.154 (doi:10.24435/materialscloud:jh-5m)

Downloaded from http://royalsocietypublishing.org/rsta/article-pdf/doi/10.1098/rsta.2024.0475/6132976/rsta.2024.0475.pdf
by guest
on 08 May 2026

59. Abidin AFZ, Saputro AG, Minggu LJ, Yunus RM, Hamada I. 2026 Supplementary material from: Effect of the OH Functionalization on the Catalytic Activity of Single-Atom Catalyst. Figshare. (doi:10.6084/m9.figshare.c.8396019)

Downloaded from http://royalsocietypublishing.org/rsta/article-pdf/doi/10.1098/rsta.2024.0475/6132976/rsta.2024.0475.pdf
by guest
on 08 May 2026